Bioconjugate Chemistry

Article

pubs.acs.org/bc

Radiolabeled Mannosylated Dextran Derivatives Bearing an NIR-Fluorophore for Sentinel Lymph Node Imaging

Maurício Morais,[†] Maria P. C. Campello,[†] Catarina Xavier,[‡] Johannes Heemskerk,[§] João D. G. Correia,[†] Tony Lahoutte,[‡,§] Vicky Caveliers,[‡,§] Sophie Hernot,[‡] and Isabel Santos*[,†]

[†]Centro de Ciências e Tecnologias Nucleares, Instituto Superior Técnico, Universidade de Lisboa, Estrada Nacional 10 (km 139,7), 2695-066 Bobadela LRS, Portugal

[‡]In Vivo Cellular and Molecular Imaging Laboratory, Vrije Universiteit Brussel, 1050 Brussels, Belgium

[§]Nuclear Medicine Department, Universitair Ziekenhuis, 1090 Brussels, Belgium

Supporting Information

ABSTRACT: Current methods for sentinel lymph node (SLN) mapping involve the use of radioactivity detection with technetium-99m sulfur colloid and/or visually guided identification using a blue dye. To overcome the kinetic variations of two individual imaging agents through the lymphatic system, we report herein on two multifunctional macromolecules, **5a** and **6a**, that contain a radionuclide (^{99m}Tc or ^{68}Ga) and a near-infrared (NIR) reporter for pre- and/or intraoperative SLN mapping by nuclear and NIR optical imaging techniques. Both bimodal probes are dextran-based polymers (10 kDa) functionalized with pyrazole-diamine (Pz) or 1,4,7,10-tetraazacyclododecane-1,4,7,10-tetra-acetic acid (DOTA) chelating units for labeling with *fac*-[^{99m}Tc(CO)$_3$]$^+$ or ^{68}Ga(III), respectively, mannose units for receptor targeting, and NIR fluorophore units for optical imaging. The probes allowed a clear visualization of the popliteal node by single-photon emission computed tomography (SPECT/CT) or positron emission tomography (PET/CT), as well as real-time optically guided excision. Biodistribution studies confirmed that both macromolecules present a significant accumulation in the popliteal node (**5a**: 3.87 ± 0.63% IA/organ; **6a**: 1.04 ± 0.26% IA/organ), with minimal spread to other organs. The multifunctional nanoplatforms display a popliteal extraction efficiency >90%, highlighting their potential to be further explored as dual imaging agents.

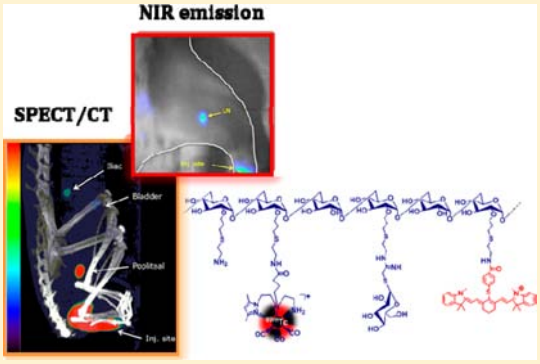

INTRODUCTION

The sentinel lymph node (SLN) is the first node receiving lymphatic drainage directly from the region of primary tumors.[1,2] The detection of SLN is regarded as useful prognostic information for some cancers, namely, melanoma, breast, lung, and colon.[3−7] After injection of a radiopharmaceutical, the SLN can be preoperatively detected by lymphoscintigraphy, whereas the surgeon can localize the SLN intraoperatively based on the acoustic signal coming from a hand-held gamma probe.[8,9] The most frequently used radiopharmaceuticals for sentinel lymph node detection (SLND), namely, ^{99m}Tc-human serum albumin colloids and filtered ^{99m}Tc-sulfur colloids, suffer from either slow clearance rate from the injection site or low residence time in the SLN.[8−13]

With the aim of designing specific probes for SLND, the mannose receptor (MR) expressed on lymphatic macrophages became an attractive target.[14,15] Indeed, conjugation of mannose molecules to ^{99m}Tc-labeled macromolecules like polylysine, albumin, dextrans, and gold nanoparticles led to compounds that can be trapped in the sentinel node with minimal spread to nontarget organs.[10,11,16−20] Among these, mannosylated ^{99m}Tc-diethylene triamine pentaacetic acid (DTPA)-dextran (^{99m}Tc-Tilmanocept) reported by Vera and co-workers has shown the most promising in vivo behavior and has been recently approved by FDA for SLND in melanoma and breast cancer.[21,22] Profiting from the versatility of the ^{99m}Tc-tricarbonyl technology as well as from the superior coordination properties of the pyrazolyl-diamine-based chelators, we have also reported the first class of fully characterized ^{99m}Tc-mannosylated dextran derivatives with adequate biological features for SLND.[10,11]

In some cases, a blue dye is coinjected with the radiopharmaceutical to obtain visual guidance during SLN surgery. However, this procedure presents some drawbacks, namely, tattooing of skin, limited value when the node is localized deep within the tissue, and different kinetics through the lymphatic system of the individual imaging agents.[23] To overcome these drawbacks, near-infrared (NIR)-emitting fluorophores have been proposed for real-time intraoperative SLND as they

Received: July 25, 2014
Revised: September 25, 2014
Published: September 29, 2014

Scheme 1. Synthesis of 5a/b and 6a/b[a]

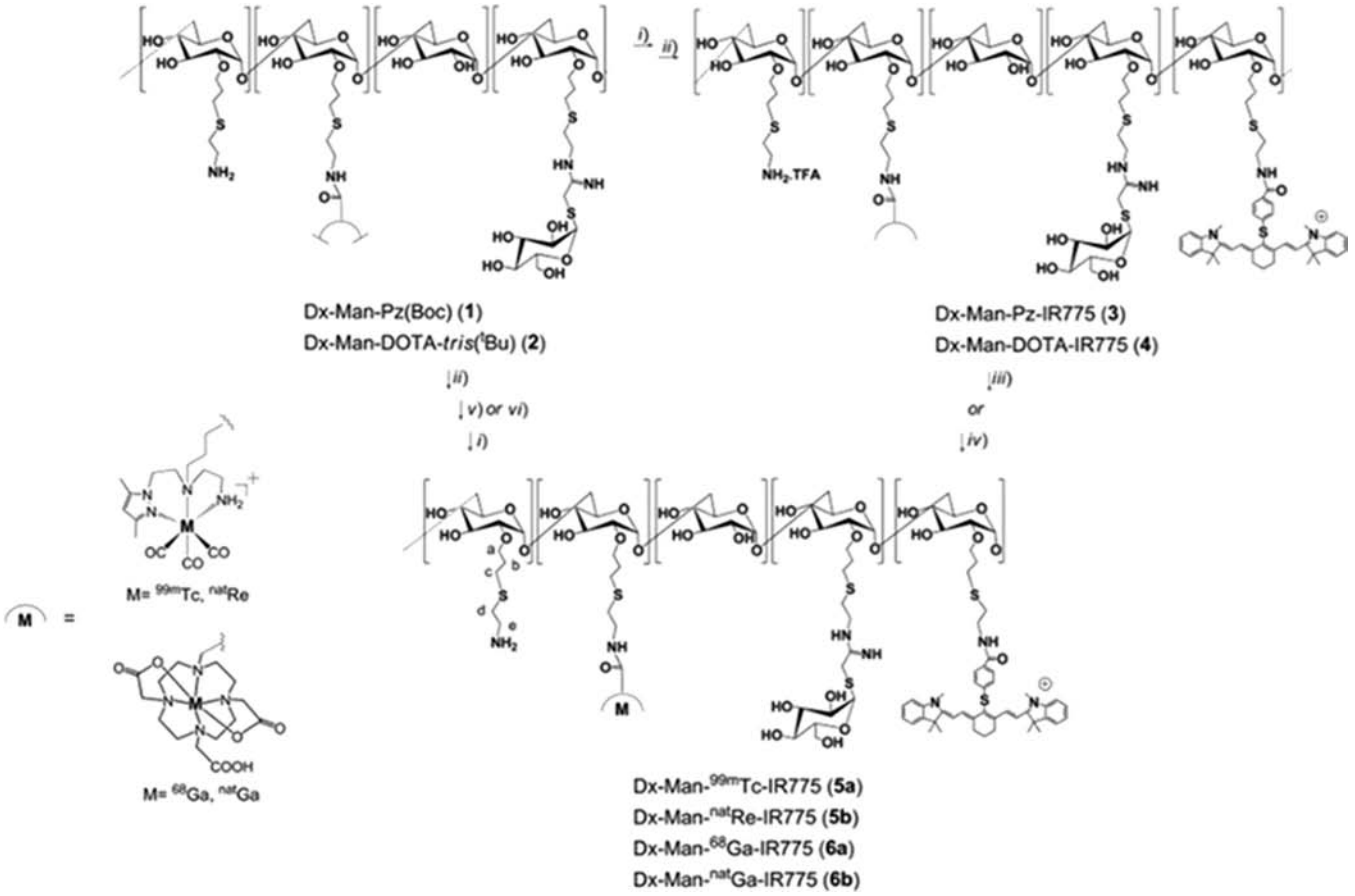

[a](i) IR755-Succ; (ii) TFA; (iii) $[^{99m}Tc(CO)_3(H_2O)_3]^+$, 100 °C, 10 min; (iv) ^{68}Ga(III), 50 °C, 15 min; (v) $[^{nat}Re(CO)_3(H_2O)_3]^+$, 50 °C, 16 h; (vi) $^{nat}Ga(NO_3)_3{\cdot}10H_2O$, 50 °C, 2 h.

present greater sensitivity and depth penetration compared to blue dyes.[24−27] Moreover, the incorporation of a NIR fluorophore and a radionuclide in the same imaging agent would enable pre- and intraoperative SLND using one single dual probe for nuclear imaging and optically guided surgery.

The extensive work of van Leeuwen and co-workers is worth noting, in which the authors have used the hybrid fluorescent−radioactive tracer indocyanine green(ICG)-^{99m}Tc-nanocolloid, a self-assembled multimodal complex in which ICG is noncovalently bound to the albumin radiocolloid, for LN imaging in various clinical trials.[24,27−30]

With regard to other families of multimodal tracers, namely, those in which the fluorescent unit is covalently attached to the radiotracer, target-specific mannosylated nanocarriers containing radionuclides (e.g., ^{18}F, ^{68}Ga, or ^{99m}Tc) and NIR fluorophores have been reported for SLN mapping.[31−34] Nevertheless, the performance of these probes for SLN mapping still has to be improved, particularly in the case of dual probes containing ^{99m}Tc and ^{68}Ga, which are among the most relevant radionuclides for single photon emission computed tomography (SPECT) and positron emission tomography (PET) imaging, respectively. Indeed, these probes still present a relatively slow clearance from the injection site or low residence time in the SLN. The promising biological results we have previously reported for $^{99m}Tc(CO)_3$-labeled mannosylated dextrans,[10] which present high SLN accumulation and high popliteal extraction values, prompted us to design new mannosylated dextran-based nanoconstructs functionalized with a NIR dye and with adequate chelators for a stable radiometal coordination. Therefore, herein, we report on the synthesis, characterization, and preclinical evaluation of $^{99m}Tc(CO)_3$- and ^{68}Ga-mannosylated dextran derivatives containing NIR fluorophores (**5a** and **6a**) for pre- and intraoperative SLN mapping.

RESULTS

The ^{99m}Tc- and ^{68}Ga-multimodal dextran-based probes were prepared, characterized from the chemical and physical point of view, and biologically evaluated as briefly described below and detailed in the Supporting Information (SI). The mannosylated dextran precursors **3** and **4** and their respective metalated nanocompounds (**5a**/**b** and **6a**/**b**) were synthesized as depicted in Scheme 1.

Compounds **3** and **4** were characterized by ^{1}H- and ^{13}C-NMR, IR, and UV−vis spectroscopy. The number of chelators, mannose, and amine units per dextran molecule in both compounds was determined based on the intensity ratios of appropriate ^{1}H NMR resonances from the different units, as previously demonstrated.[10] The number of fluorophore units per molecule of dextran in **3**, **4**, **5b**, and **6b** was determined by UV−vis spectrophotometry as described in the SI. Brought together, these studies allowed the determination of the substitution degree of the dextran backbone that is summarized in Table 1.

dx.doi.org/10.1021/bc500336a | Bioconjugate Chem. 2014, 25, 1963−1970

Table 1. Group Density, Hydrodynamic Diameter (*Z*-average), Zeta Potential (Zp), and Calculated Molecular Weight of Dextran Derivatives

	group density (units/molecule dextran)						
compounds	amine	chelator	mannose	fluorophore	*Z*-average (nm)[a]	Zp (mV)[a]	MW calculated (g/mol)[b]
Dextran	-	-	-	-	4.3 ± 0.4	−9.9 ± 0.5	10000
3	6	8	13	3	17.7 ± 2.0	−2.3 ± 0.4	22116
4	7	5	15	3	11.3 ± 1.4	−4.8 ± 0.1	19918
5b	6	8	13	3	22.5 ± 2.9	−7.7 ± 2.5	23364
6b	7	5	15	3	50.8 ± 8.1	−2.9 ± 0.3	21392

[a]Mean ± SD. [b]MW was estimated according to the substitution degree of the polymer found by ^{1}H NMR and UV−vis spectrophotometry.

The purity of all dextran-based polymers (>95%) was evaluated by SEC and RP-HPLC at 220 and 760 nm. Figure 1 displays the SEC−UV−vis traces of the conjugates **3** and **4** at 220 and 760 nm.

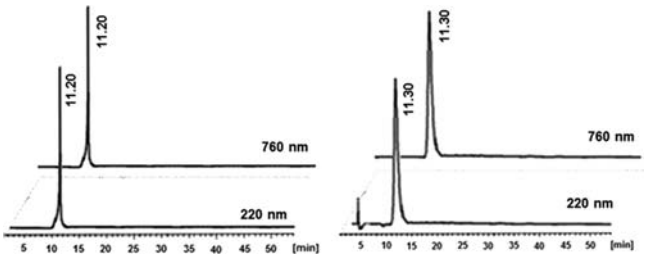

Figure 1. SEC chromatograms of **3** (left) and **4** (right) at λ = 220 and 760 nm.

The physical features of the dextran derivatives, namely, their hydrodynamic diameter and zeta potential, have been determined by DLS and LDV (Table 1). The dextran conjugates **3** (*Z*-average = 17.7 ± 2.0 nm) and **4** (*Z*-average = 11.3 ± 1.4 nm) present larger hydrodynamic diameters than the dextran precursor (*Z*-average = 4.3 ± 0.4 nm). Upon metalation, these polymeric conjugates also yielded compounds with larger hydrodynamic diameters (**5b**, *Z*-average = 22.5 ± 2.9 nm; **6b**, *Z*-average = 50.8 ± 8.1 nm). Noteworthy is the fact that no relevant changes in the zeta potential of the dextran derivatives have been observed, compared to dextran alone. Indeed, they all have a slightly negative superficial charge, with values between −2.3 ± 0.4 and −7.7 ± 2.5 mV.

The bimodal probes **5a** and **6a** were prepared by reacting **3** and **4** with the precursors *fac*-$[^{99m}Tc(CO)_3(H_2O)_3]^+$ and ^{68}Ga(III), respectively (Scheme 1). Incorporation of the radiometals reached more than 95% with specific activities in the range 19.4−23.2 MBq/nmol and 34.4−42.1 MBq/nmol for **5a** and **6a**, respectively. In both cases, only one species was formed as demonstrated by RP-HPLC (**5a**: t_R = 15.4 min; **6a**: t_R = 16.1 min).

The chemical identity of **5a** and **6a** was confirmed by comparing their retention times in the RP-HPLC chromatograms (γ-detection) with those of the respective nonradioactive surrogates **5b** and **6b** (UV detection) (Figure 2).

The impact of the labeling conditions on the fluorescence properties of **5a** and **6a** was assessed by comparing the emitted fluorescence signals of equal volumes (20 μL) of equimolar solutions of **3**, **5a**, **4**, and **6a** applied on a ITLC-SG plate. The fluorescence signal of the samples was measured in a Odyssey IR imaging system using the 800 nm channels. These assays have shown that **5a** and **6a** have fluorescent properties

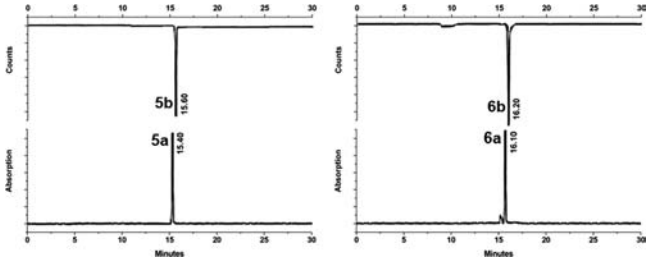

Figure 2. RP-HPLC chromatograms of **5a**/**b** and **6a**/**b** (the short difference in the retention times of the radioactive nanocompounds and respective cold surrogates is due to detector separation).

comparable to the ones exhibited by the respective precursors **3** and **4**.

The bimodal probe **5a** is highly stable in vitro, as shown by its resistance toward transchelation reactions with strong competitors such as cysteine and histidine (>95% purity after 6 h incubation) and the absence of pertechnetate, even after long incubation periods of time at 37 °C. This result is in line with the well-established ability of the pyrazolyl-diamine chelating unit to stabilize the *fac*-$[^{99m}Tc(CO)_3]^+$ core.[10,35−37]

The stability of **6a** was not assessed directly, but the congener **6c** (SI) is highly stable, remaining intact after incubation with excess of transferrin or DTPA up to 6 h at 37 °C (>96% purity as determined by ITLC-SG).

Planar gamma-images and SPECT/CT images (Figure 3) acquired, respectively, at 60 and 90 min after injection of **5a** demonstrated that the tracer migrates from the injection site to the popliteal lymph node with a slight spread to secondary lymph nodes. Low signal is observed in the liver and bladder.

The popliteal lymph node in Wistar rat could also be visualized by PET/CT imaging 60 min after subcutaneous injection of **6a**. As can be also seen in Figure 4, only a slight spread to secondary lymph nodes was found.

The imaging results were confirmed by ex vivo biodistribution analysis performed at 180 and 90 min p.i. for **5a** and **6a**, respectively (Table 2). In both cases, a significant accumulation in the popliteal lymph node was found (**5a**: 3.87 ± 0.63% IA/organ and **6a**: 1.04 ± 0.26% IA/organ).

Injection of **5a** or **6a** (1 nmol) allowed a clear visualization of the popliteal lymph node by NIR fluorescence imaging (Figure 5). Furthermore, the optical signal of **5a** and **6a** enabled a simple image-guided surgical excision of the lymph node (SI).

■ DISCUSSION

We have previously reported a stable $^{99m}Tc(CO)_3$-mannosylated dextran derivative (Dx-Man-^{99m}Tc) with adequate biological properties for SLN mapping.[10] Following this encouraging result, we synthesized and characterized the

dx.doi.org/10.1021/bc500336a | *Bioconjugate Chem.* 2014, 25, 1963−1970

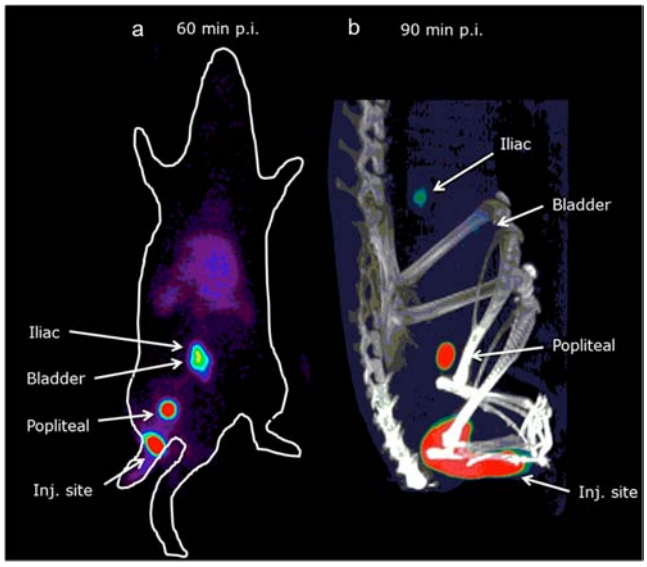

Figure 3. Planar gamma-image of a Wistar rat injected with **5a** at 60 min p.i. (a). SPECT/CT image of the same animal at 90 min p.i. (b).

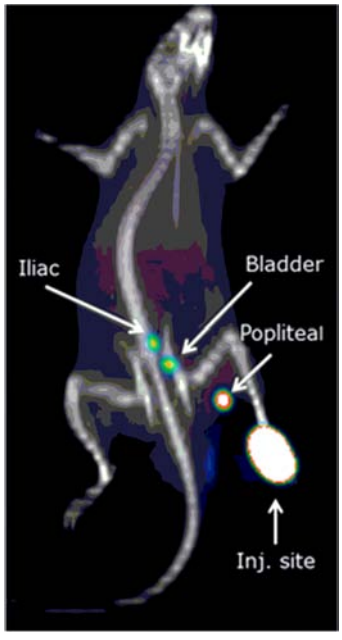

Figure 4. PET/CT image of a Wistar rat injected with **6a** at 60 min p.i.

dextran-based (~10 kDa) bimodal probe **5a** containing the $^{99m}Tc(CO)_3$ core for SPECT and a IR775-derived NIR-fluorophore for optical imaging. The metal core is stabilized by a pyrazole-diamine chelating backbone (Pz), which is known to give highly stable complexes in vitro and in vivo, and has been successfully used for labeling a wide range of biologically active biomolecules.[35−37] Aiming to profit from the widespread availability of ^{68}Ga through a $^{68}Ge/^{68}Ga$ generator and from its superior imaging properties for PET, we have also prepared and characterized the bimodal probe **6a** in which 1,4,7,10-tetraazacyclododecane-1,4,7,10-tetraacetic acid (DOTA) was used for metal stabilization. Although acyclic chelators, such as diethylenetriaminepentaacetic acid (DTPA), have been used to stabilize Ga(III)-complexes it is well recognized that cyclic chelators, namely, DOTA, can afford Ga-complexes of high kinetic inertness and thermodynamic stability that show a high

Table 2. Biodistribution Studies of 5a and 6a in Wistar Rat Model at 180 and 90 min, Respectively (n = 3)

	5a	6a
	%IA/Organ	%IA/Organ
organ	180 min	90 min
liver	1.81 ± 0.46	1.48 ± 0.15
intestine	0.34 ± 0.17	0.09 ± 0.08
stomach	0.01 ± 0.01	0.08 ± 0.01
kidney	0.46 ± 0.1	0.35 ± 0.15
bladder	0.02 ± 0.01	0.14 ± 0.02
muscle	0.03 ± 0.02	0.18 ± 0.04
spleen	0.02 ± 0.01	0.01 ± 0.00
blood	0.23 ± 0.20	1.36 ± 0.54
popliteal node	3.87 ± 0.63	1.04 ± 0.26
iliac node	0.40 ± 0.20	0.10 ± 0.54
site of inj.	86.73 ± 0.92	92.82 ± 0.94
PE (%)	89.66 ± 1.22	91.01 ± 1.35

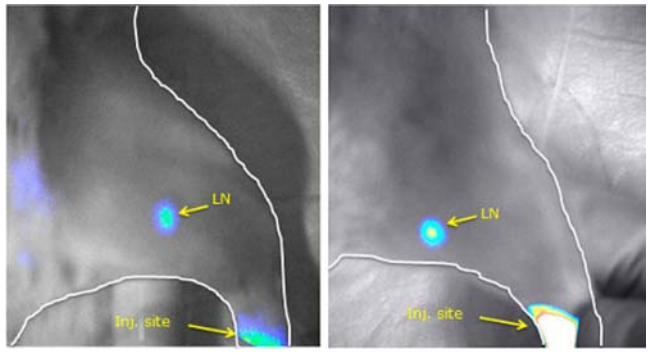

Figure 5. NIR optical images of Wistar rat leg injected with **5a** (left, 180 min p.i.) or **6a** (right, 90 min p.i.) respectively. The yellow arrows indicate the localization of the bimodal probes in the popliteal lymph node.

resistance to in vivo transchelation processes if compared with the DTPA counterparts.[38−40]

The probes **5a** and **6a** described herein were prepared and characterized aiming to be used for preoperative SLN mapping by SPECT or PET imaging and also for optical image-guided excision. Their administration avoids separate injections of a radiopharmaceutical and a blue dye, and may allow a one-to-one correlation between pre- and intraoperatively localization of the SLN. These probes were characterized by comparing their chromatographic behavior with that of the surrogates **5b** and **6b**, respectively, which were synthesized and fully characterized from the physicochemical point of view. The multimodal probes **5a** and **6a** present a similar substitution pattern of the dextran backbone (Table 1). A comparison with other ^{99m}Tc- or ^{68}Ga-dextran-based bimodal probes is difficult, as for some of them there is no data available (^{99m}Tc-labeled Cy7 tilmanocept) and for other different chelators and/or fluorescent reporter moieties have been used (^{68}Ga-labeled 800CW-tilmanocept).[33] The hydrodynamic diameter and zeta potential described in this work for **5a** and **6a** cannot be also directly compared to ^{99m}Tc-labeled tilmanocept or any other dextran-based bimodal probes such as ^{99m}Tc-labeled Cy7 tilmanocept, [^{18}F]PET/NIR-Lymphoseek, or ^{68}Ga-labeled 800CW-tilmanocept, as no physical characterization is available.[19,31−33] In our work we have considered that the hydrodynamic diameters and zeta potential values of the

dx.doi.org/10.1021/bc500336a | Bioconjugate Chem. 2014, 25, 1963−1970

radioactive compounds are similar to the ones found for the corresponding nonradioactive analogues **5b** (*Z*-average = 22.5 ± 2.9 nm; Zp = −7.7 ± 2.5 mV) and **6b** (*Z*-average = 50.8 ± 8.1 nm; Zp = −2.9 ± 0.3 mV).

The sizes found for these probes are 10- to 4-fold smaller than the values described for the ^{99m}Tc-colloids in clinical setting (200 nm).[8,13,22] However, the *Z*-average values found for both probes are large enough to prevent leakage from the interstitial space to the circulatory system.

The SLN-mapping properties of **5a** or **6a** were assessed in Wistar rats after subcutaneous administration. Dynamic planar images have shown relevant migration of **5a** from the injection site, with accumulation of radioactivity in the popliteal node. Low activity was detected in the iliac lymph node (Figure 3A). Similar results were obtained from the SPECT/CT images at 180 min p.i. (Figure 3B), where a clear delineation of the popliteal node with minimal spread to secondary lymph nodes or nontarget organs was observed. As shown in Figure 4, similar results were obtained for PET/CT imaging of **6a** at 60 min p.i.

The ex vivo biodistribution data for both probes corroborate the results obtained by the nuclear imaging techniques with appreciable accumulation of **5a** (3.87 ± 0.63% IA/organ) and **6a** (1.04 ± 0.26% IA/organ) in the popliteal lymph node at 180 and 90 min, respectively. The uptake of each probe in nontargeted organs was negligible (<0.5% IA/organ), except for blood (^{99m}Tc: 0.23 ± 0.20; ^{68}Ga:1.36 ± 0.54% IA/organ) and liver (^{99m}Tc: 1.81 ± 0.46; ^{68}Ga:1.48 ± 0.15% IA/organ), which present slightly higher values. These values may be due to the interaction of the macromolecule with the MR's expressed by Kupffer cells in liver.[41]

Surprisingly, no information regarding the activity retained at the injection site is available for the dextran-based bimodal tracers' ^{99m}Tc-labeled Cy7 tilmanocept or ^{68}Ga-labeled 800CW-tilmanocept.[32,33] However, the values found for both probes described herein (**5a**, 86.73 ± 0.92% IA, 180 min; **6a**, 92.82 ± 0.94% IA, 90 min) are higher than the values found for compounds in clinical use, such as ^{99m}Tc-sulfur colloid (70.4 ± 11.0% IA) and Lymphoseek (52.6 ± 10.5% IA).[19] The moderate clearance from the injection site found for our compounds may be due to the low zeta potential values (**5a**, Zp = −7.7 ± 2.5 mV; **6a**, Zp = −2.9 ± 0.3 mV). In fact, previously reported results demonstrated that when the absolute value of zeta potential is less than 10 mV the repulsive forces between particles is weak leading to in vivo aggregation and hampering a fast migration from the injection site.[42]

Although the biological data described for both bimodal probes cannot be compared directly with other tracers explored for SLND, as the latter were evaluated in different animal models, the popliteal extraction (PE) value found for **5a** (89.66 ± 1.22%) compares well with the ones found for ^{99m}Tc-labeled tilmanocept in rabbits (90.1 ± 10.7%), ^{99m}Tc-labeled Cy7 tilmanocept in mice (83 ± 11%), and is much higher than the value described for ^{99m}Tc-labeled colloids (78.8 ± 6.5%) at 180 min p.i.[19,32,43]

The PE value found for **6a** (91.00 ± 1.35%) at 90 min p.i. is also comparable with the one found for the bimodal tracer [^{18}F]PET/NIR-Lymphoseek (ca. 87 ± 7%, 80 min p.i.) in mice.[31] Taken together, these results demonstrate the potential usefulness of the described bimodal probes for preoperative planning using SPECT/CT or PET/CT imaging.

The fluorescence signal of each probe, monitored with an imaging camera (Fluobeam), allowed also the real-time guide surgical exposure, visual identification, and excision of the SLN (video in SI). Furthermore, histological examination of the first LN on a EVOS FI (digital fluorescence microscope) has shown a homogeneous distribution of fluorescence in a section (see SI).

Considering the rapid migration and persistent retention in the popliteal node as well as the low distal lymph node accumulation, we consider that after an optimization process, namely, through replacement of IR-775 by an FDA-approved NIR fluorophore such as ICG, both probes hold the potential to be explored in the two conventional protocols currently used for SLN detection (1- or 2-day protocol). Only a single injection by the nuclear medicine physician is required for both preoperative mapping and intraoperative SLND, reducing the duration of surgery, anesthesia, and cost. Furthermore, accurate identification and excision of the SLN will decrease the postoperative morbidity rates, improving the patients' quality of life.[8,26,44]

■ CONCLUSIONS

With the aim of designing bimodal tracers for SLND by nuclear and NIR optical imaging we have prepared and fully characterized ^{99m}Tc(CO)$_3$- and ^{68}Ga-labeled mannosylated dextran derivatives containing NIR fluorophore units (**5a** and **6a**). Herein we provided solid information on the physicochemical properties of nanotracers for SLND and correlate these features with the in vivo properties. The bimodal probes show a clear delineation of the SLN without significant washout to other regions as shown by SPECT/CT and PET/CT imaging. Furthermore, the NIR reporter of both probes enabled intraoperative guidance and visual identification of the SLN during surgery. The biological properties of these probes highlight their potential to be further explored as dual imaging agents for SLND using SPECT/NIR or PET/NIR. Finally, profiting from the ability of the DOTA chelator to provide inert complexes with a large variety of trivalent radiometals, the multifunctional nanoplatform **4** can be labeled with many other radionuclides, such as ^{89}Zr (PET/NIR), ^{67}Ga, or ^{111}In (SPECT/CT-NIR).

■ MATERIAL AND METHODS

All chemicals were of reagent grade and used without further purification. Solvents for high-performance liquid chromatography (HPLC) were HPLC-grade. Dextran (9500−10 500 g/mol) and mannose were purchased from Sigma-Aldrich. Tri-*tert*-butyl 2,2′,2″-(10-(2-2,5-dioxopyrrolidin-1-yl)oxy)-2-oxoethyl)-1,4,7,10-tetra-aza-cyclododecane-1,4,7-triyl)triacetate (DOTA-tris(^{t}Bu)-NHS ester) was purchased from CheMatech. 2-[2-[2-Chloro-3-[2-(1,3-dihydro-1,3,3-trimethyl-2*H*-indol-2-ylidene)-ethylidene]-1-cyclohexen-1-yl]-ethenyl]-1,3,3-trimethyl-3*H*-indolium chloride (IR775.Cl, excitation and emission maximum: 793 and 818 nm, respectively) was purchased from Sigma-Aldrich. The polymeric precursors Dx-Man-Pz(Boc) (**1**) and Dx-Man-^{nat}Re were prepared according to described methods.[10] Dx-Man-DOTA-tris(^{t}Bu) (**2**), IR775-Succ, Dx-Man-Pz-IR775 (**3**), and Dx-Man-DOTA-IR775 (**4**) were prepared and characterized as described in Supporting Information (SI). Natural gallium, as Ga(NO$_3$)$_3$·10H$_2$O, was purchased from Sigma-Aldrich. The radioactive precursor [^{99m}Tc(CO)$_3$(H$_2$O)$_3$]$^+$ was prepared as previously described.[10] ^{68}Ga(III) was obtained from a ^{68}Ge/^{68}Ga generator (Eckert and Ziegler) eluted with 0.1 M HCl (made from 30% HCl ultrapure from Merck). ^{67}GaCl$_3$ was prepared from ^{67}Ga-citrate

dx.doi.org/10.1021/bc500336a | *Bioconjugate Chem.* 2014, 25, 1963−1970

(Mallinckrodt Medical, Netherlands) as described in the literature.[45] Buffers used for coupling reactions or radiolabeling were purified from metal contamination using Chelex 100 resin (Sigma-Aldrich). ^{1}H- (300 MHz) and ^{13}C- (75.5 MHz) NMR spectra were recorded in a Varian Unit Inova-300 spectrometer at 20 °C. ^{71}Ga-NMR spectra were recorded using a Bruker Avance 500 (11.75-T, 152.5-MHz) spectrometer at 25 °C. Infrared (IR) spectra were recorded as KBr pellets on a Bruker Tensor 27 Fourier transform IR spectrometer in the region 4000−400 cm^{-1} (SI for details). Reversed-phase HPLC (RP-HPLC) and size exclusion chromatography (SEC) analysis were performed using a PerkinElmer liquid chromatography pump 200 coupled to a UV/vis detector (220 and 760 nm, Shimadzu SPD-10 AV or PerkinElmer Lc 290) and γ detector (LB 507 or LB 509, Berthold). RP-HPLC was performed using a Supelco Discovery Bio Wide Pore C18 25 cm × 4.6 mm, 5 μm analytical column; flow: 1 mL/min; eluents: A - TFA 0.1% in H_2O; B - TFA 0.1% in CH_3CN. Gradient: 0−9 min, 0−80% B; 9−14 min, 80% B; 14−15 min, 80−0% B; 15−20 min, 0% B. SEC was performed using a Shodex OHpack SB-803 HQ analytical column; flow: 0.5 mL/min; isocratic elution: 0−60 min, 100% H_2O (0.02% NaN_3). Instant thin layer chromatography (ITLC) analysis of **5a** or Dx-Man-^{68}Ga-IR775 (**6a**) was performed in silica gel impregnated glass fiber sheets (Pall Corporation, Life Sciences) eluted with 5% HCl 6 M/MeOH or sodium citrate 0.1 M (pH 5.0), respectively. Radioactivity detection on ITLC was performed with a radiochromatograph (Berthold LB 2723) equipped with a 20-mm-diameter NaI(Tl) scintillation crystal.

The average hydrodynamic diameter (*Z*-average) and zeta potential (Zp) of the nanocompounds were determined by dynamic light scattering (DLS) and laser Doppler velocimetry (LDV) in zeta potential cells using a Zeta Sizer Nano ZS from Malvern (SI).

Synthesis of Dx-Man-^{99m}Tc-IR775 (5a) and Dx-Man-$^{68/67}$Ga-IR775 (6a/6c). Compound **5a** was prepared by adding 1 mL of *fac*-$[^{99m}Tc(CO)_3(H_2O)_3]^+$ (74−222 MBq) to a capped nitrogen purged glass vial containing **3** (100 μg, 5 nmol) and incubated for 10 min at 90 °C. Compounds **6a** and **6c** were prepared by adding 500 μL of $^{67}GaCl_3$ or ^{68}Ga(III) (198−221 MBq), at pH 5, to **4** (100 μg, 5 nmol) and incubated for 15 min at 50 °C. The labeling yield and radiochemical purity of the radiolabeled compounds were monitored by RP-HPLC, SEC, and by ITLC. $[^{99m}Tc(CO)_3(H_2O)_3]^+$, $[^{99m}TcO_4]^-$, and $^{67/68}Ga^{3+}$ precursors migrate to the solvent front (R_f = 1), whereas radioactive nanoconjugates and colloidal species stay at the origin (R_f = 0).

Synthesis of Dx-Man-^{nat}Re-IR775 (5b) and Dx-Man-^{nat}Ga-IR775 (6b). The "cold" references **5b** and **6b** were synthesized by reaction of the respective metalated precursors Dx-Man-^{nat}Re[10] and Dx-Man-^{nat}Ga with the activated NIR fluorophore ester (SI).

In Vitro Stability Studies. The in vitro stability of **5a** was assessed in the presence of a large molar excess (100-fold) of cysteine or histidine solutions as described in the SI. The stability of **6c** was assessed by incubating the compound with excess (100-fold) of transferrin or DTPA as described in the SI.

Animal Studies. The ethical committee of the Vrije Universiteit Brussel approved all animal study protocols. Female Wistar rats (n = 3 per group) weighing 200−250 g were anesthetized by intraperitoneal injection of Nembutal (0.1 mL of 60 mg/mL solution per 100 g bodyweight) and the left leg region was shaved. Approximately 50 μL (20 μg, 1 nmol) of **5a** or **6a** (19−23 MBq) was injected subcutaneously in the left footpad region. The area of injection was massaged gently with a strip of gauze pad for about 2 min to facilitate movement of the radiolabeled preparation from the injection site. After injection of the ^{99m}Tc-labeled probe, the animals were subjected to a dynamic scintigraphy scan over 60 min. At 90 min postinjection (p.i.) a SPECT/CT image was acquired. Animals injected with the ^{68}Ga-labeled probe underwent a PET/CT scan at 60 min p.i.

The animals were sacrificed at 180 and 90 min p.i. in the case of ^{99m}Tc- or ^{68}Ga-labeled probes, respectively. The relevant organs and tissues, including popliteal and iliac lymph node, were harvested for ex vivo biodistribution analysis. Radioactivity retained in each organ or tissue was measured on a gamma-counter (Cobra II inspector 5003, Canberra-Packard), decay-corrected, and expressed as a percentage of the total injected activity per organ (% IA). The popliteal extraction (PE) was determined as previously described, considering the accumulated radioactivity at the popliteal and iliac lymph node.[10,46]

Nuclear Imaging Techniques. *Dynamic Scintigraphy.* Animals were placed in prone position under a gamma camera (E.cam^{180}, Siemens Medical Solutions) equipped with a parallel-hole collimator (256 × 256 matrix, zoom factor 1.78). The site of injection was for the greater part shielded with lead during the acquisition. Consecutive images of 30 s each were acquired and further processed in AMIDE medical software.

SPECT/CT Imaging. Micro-CT imaging was performed prior to SPECT with a dual-source CT-scanner (Skyscan 1178; Skyscan) at 60 kV and 615 mA, with a resolution of 83 μm. Images were reconstructed by filtered back projection (NRecon; Skyscan). Pinhole SPECT was performed with a dual-headed gamma-camera (e.cam^{180}), equipped with two single pinhole collimators (1.5 mm; distance between rotation axis and detector surface 270 mm). Images were acquired in 64 projections with 10 s per step over 360° (zoom 1, 128 × 128 matrix). Images were reconstructed by iterative reconstruction algorithm and fused with the micro-CT images. Images were analyzed in Osirix.

PET/CT Imaging. Image acquisition was performed on a clinical Gemini time-of-flight PET/CT scanner (Philips) at 1 h after injection. The CT acquisition was set to 120 kV at 83 mA at a resolution of 5 mm, using filtered back projection for image reconstruction. The total CT scanning time was 10 s. PET images were acquired over 9 min and reconstructed to 426 slices of 128 × 128 pixels (at a 2 mm isotropic pixel size), with attenuation correction based on the CT data. The images were analyzed using Osirix.

NIR Fluorescence Imaging. Camera FluoBeam800 (Fluoptics) was used for NIR imaging of the left leg at 180 or 90 min after injection of 1 nmol of **5a** or **6a**, respectively. Image processing was performed using ImageJ software. The NIR signal was also used as guidance for the precise excision of the popliteal lymph node after sacrifice of the animals.

■ ASSOCIATED CONTENT

Ⓢ Supporting Information

Synthetic experimental procedures and characterization (^{1}H- and ^{13}C NMR, IR, or emission spectrum) of dextran derivatives (Dx-DOTA-tris(^{t}Bu), **2**, Dx-Man-DOTA, **IR775-Succ**, **3**, **4**, Dx-Man-^{nat}Ga, **5b**, **6b**), additional details on in vitro stability studies, experimental details to collect emission spectrum and real time optical-guided excision of LN are available. This

material is available free of charge via the Internet at http://pubs.acs.org.

AUTHOR INFORMATION

Corresponding Author

*E-mail: isantos@ctn.ist.utl.pt. Phone: +351219946201.

Notes

The authors declare no competing financial interest.

ACKNOWLEDGMENTS

The Fundação para a Ciência e Tecnologia (FCT) is acknowledged for financial support (EXCL/QEQ-MED/0233/2012). M. Morais thanks FCT for a Ph.D. fellowship (SFRH/BD/48066/2008). Covidien-Mallinckrodt is acknowledged for the IsoLink kits. COST Action TD1004 is acknowledged for the STSM-TD1004-040213-027456.

REFERENCES

(1) Morton, D. L., and Chan, A. D. (2000) The concept of sentinel lymph node localization: How it started. *Semin. Nucl. Med. 30*, 4−10.

(2) Alitalo, A., and Detmar, M. (2012) Interaction of tumor cells and lymphatic vessels in cancer progression. *Oncogene 31*, 4499−508.

(3) Leong, S. P., Nakakura, E. K., Pollock, R., Choti, M. A., Morton, D. L., Henner, W. D., Lal, A., Pillai, R., Clark, O. H., and Cady, B. (2011) Unique patterns of metastases in common and rare types of malignancy. *J. Surg. Oncol. 103*, 607−14.

(4) Shayan, R., Achen, M. G., and Stacker, S. A. (2006) Lymphatic vessels in cancer metastasis: bridging the gaps. *Carcinogenesis 27*, 1729−1738.

(5) Veronesi, U., Galimberti, V., Zurrida, S., Pigatto, F., Veronesi, P., Robertson, C., Paganelli, G., Sciascia, V., and Viale, G. (2001) Sentinel lymph node biopsy as an indicator for axillary dissection in early breast cancer. *Eur. J. Cancer 37*, 454−458.

(6) Alex, J. C. (2004) The application of sentinel node radiolocalization to solid tumors of the head and neck: A 10-year experience. *Laryngoscope 114*, 2−19.

(7) Torne, A., and Puig-Tintore, L. M. (2004) The use of sentinel lymph nodes in gynaecological malignancies. *Current Opinion in Obstetrics and Gynecology 16*, 57−64.

(8) Sharma, R., Wendt, J. A., Rasmussen, J. C., Adams, K. E., Marshall, M. V., and Sevick-Muraca, E. M. (2008) New horizons for imaging lymphatic function. *Lymphatic Continuum Revisited 1131*, 13−36.

(9) Ravizzini, G., Turkbey, B., Barrett, T., Kobayashi, H., and Choyke, P. L. (2009) Nanoparticles in sentinel lymph node mapping. *WIREs Nanomedicine and Nanobiotechnology 1*, 610−623.

(10) Morais, M., Subramanian, S., Pandey, U., Samuel, G., Venkatesh, M., Martins, M., Pereira, S., Correia, J. D. G., and Santos, I. (2011) Mannosylated dextran derivatives labeled with fac-$[M(CO)_3]^+$ (M = Tc-99m, Re) for specific targeting of sentinel lymph node. *Mol. Pharmaceutics 8*, 609−620.

(11) Pirmettis, I., Arano, Y., Tsotakos, T., Okada, K., Yamaguchi, A., Uehara, T., Morais, M., Correia, J. D. G., Santos, I., Martins, M., Pereira, S., Triantis, C., Kyprianidou, P., Pelecanou, M., and Papadopoulos, M. (2012) New Tc-99m$(CO)_3$ mannosylated dextran bearing s-derivatized cysteine chelator for sentinel lymph node detection. *Mol. Pharmaceutics 9*, 1681−1692.

(12) Eshima, D., Fauconnier, T., Eshima, L., and Thornback, J. R. (2000) Radiopharmaceuticals for lymphoscintigraphy: Including dosimetry and radiation considerations. *Semin Nucl. Med. 30*, 25−32.

(13) Wilhelm, A. J., Mijnhout, G. S., and Franssen, E. J. F. (1999) Radiopharmaceuticals in sentinel lymph-node detection - an overview. *Eur. J. Nucl. Med. 26*, S36−S42.

(14) Petrova, T. V., Makinen, T., Makela, T. P., Saarela, J., Virtanen, I., Ferrell, R. E., Finegold, D. N., Kerjaschki, D., Yla-Herttuala, S., and Alitalo, K. (2002) Lymphatic endothelial reprogramming of vascular endothelial cells by the Prox-1 homeobox transcription factor. *EMBO J. 21*, 4593−4599.

(15) Marttila-Ichihara, F., Turia, R., Miiluniemi, M., Karikoski, M., Maksimow, M., Niemela, J., Martinez-Pomares, L., Salmi, M., and Jalkanen, S. (2008) Macrophage mannose receptor on lymphatics controls cell trafficking. *Blood 112*, 64−72.

(16) Takagi, K., Uehara, T., Kaneko, E., Nakayama, M., Koizumi, M., Endo, K., and Arano, Y. (2004) Tc-99m-labeled mannosyl-neoglycoalbumin for sentinel lymph node identification. *Nucl. Med. Biol. 31*, 893−900.

(17) Vera, D. R., Wisner, E. R., and Stadalnik, R. C. (1997) Sentinel node imaging via a nonparticulate receptor-binding radiotracer. *J. Nucl. Med. 38*, 530−5.

(18) Jeong, J. M., Hong, M. K., Kim, Y. J., Lee, J., Kang, J. H., Lee, D. S., Chung, J. K., and Lee, M. C. (2004) Development of Tc-99m-neomannosyl human serum albumin (Tc-99m-MSA) as a novel receptor binding agent for sentinel lymph node imaging. *Nucl. Med. Commun. 25*, 1211−1217.

(19) Vera, D. R., Wallace, A. M., and Hoh, C. K. (2001) [(99m)Tc]MAG(3)-mannosyl-dextran: a receptor-binding radiopharmaceutical for sentinel node detection. *Nucl. Med. Biol. 28*, 493−8.

(20) Ocampo-Garcia, B. E., Ramirez, F. D., Ferro-Flores, G., De Leon-Rodriguez, L. M., Santos-Cuevas, C. L., Morales-Avila, E., de Murphy, C. A., Pedraza-Lopez, M., Medina, L. A., and Camacho-Lopez, M. A. (2011) Tc-99m-labelled gold nanoparticles capped with HYNIC-peptide/mannose for sentinel lymph node detection. *Nucl. Med. Biol. 38*, 1−11.

(21) Newsbriefs. *J. Nucl. Med.* (2013) *54*, 19N−21N.

(22) Eckelman, W. C., Jones, A. G., Duatti, A., and Reba, R. C. (2013) Progress using Tc-99m radiopharmaceuticals for measuring high to low capacity sites. *Drug Discovery Today 18*, 984−991.

(23) Newman, E. A., and Newman, L. A. (2007) Lymphatic mapping techniques and sentinel lymph node biopsy in breast cancer. *Surg. Clin. North Am. 87*, 353−+.

(24) van den Berg, N. S., Valdes-Olmos, R. A., van der Poel, H. G., and van Leeuwen, F. W. (2013) Sentinel lymph node biopsy for prostate cancer: a hybrid approach. *J. Nucl. Med. 54*, 493−6.

(25) Culver, J., Akers, W., and Achilefu, S. (2008) Multimodality molecular imaging with combined optical and SPECT/PET modalities. *J. Nucl. Med. 49*, 169−172.

(26) Vahrmeijer, A. L., Hutteman, M., van der Vorst, J. R., van de Velde, C. J., and Frangioni, J. V. (2013) Image-guided cancer surgery using near-infrared fluorescence. *Nat. Rev. Clin. Oncol. 10*, 507−518.

(27) Van den Berg, N. S., Buckle, T., Kleinjan, G. I., Klop, W. M., Horenblas, S., Van der Poel, H. G., Valdes-Olmos, R. A., and Van Leeuwen, F. I. (2014) Hybrid tracers for sentinel node biopsy. *Quarterly Journal of Nuclear Medicine and Molecular Imaging 58*, 193−206.

(28) Brouwer, O. R., van den Berg, N. S., Matheron, H. M., van der Poel, H. G., van Rhijn, B. W., Bex, A., van Tinteren, H., Olmos, R. A. V., van Leeuwen, F. W. B., and Horenblas, S. (2014) A hybrid radioactive and fluorescent tracer for sentinel node biopsy in penile carcinoma as a potential replacement for blue dye. *European Urology 65*, 600−609.

(29) Matheron, H. M., van den Berg, N. S., Brouwer, O. R., KleinJan, G. H., van Driel, W. J., Trum, J. W., Vegt, E., Kenter, G., van Leeuwen, F. W. B., and Olmos, R. A. V. (2013) Multimodal surgical guidance towards the sentinel node in vulvar cancer. *Gynecologic Oncology 131*, 720−725.

(30) Schaafsma, B. E., Verbeek, F. P. R., Rietbergen, D. D. D., van der Hiel, B., van der Vorst, J. R., Liefers, G. J., Frangioni, J. V., van de Velde, C. J. H., van Leeuwen, F. W. B., and Vahrmeijer, A. L. (2013) Clinical trial of combined radio- and fluorescence-guided sentinel lymph node biopsy in breast cancer. *Br. J. Surg. 100*, 1037−1044.

(31) Ting, R., Aguilera, T. A., Crisp, J. L., Hall, D. J., Eckelman, W. C., Vera, D. R., and Tsien, R. Y. (2010) Fast F-18 labeling of a near-infrared fluorophore enables positron emission tomography and optical imaging of sentinel lymph nodes. *Bioconjugate Chem. 21*, 1811−1819.

(32) Emerson, D. K., Limmer, K. K., Hall, D. J., Han, S. H., Eckelman, W. C., Kane, C. J., Wallace, A. M., and Vera, D. R. (2012) A receptor-targeted fluorescent radiopharmaceutical for multireporter sentinel lymph node imaging. *Radiology 265*, 186−193.
(33) Qin, Z., Hall, D. J., Liss, M. A., Hoh, C. K., Kane, C. J., Wallace, A. M., and Vera, D. R. (2013) Optimization via specific fluorescence brightness of a receptor-targeted probe for optical imaging and positron emission tomography of sentinel lymph nodes. *J. Biomed. Opt. 18*, 101315.
(34) Stroup, S. P., Kane, C. J., Farchshchi-Heydari, S., James, C. M., Davis, C. H., Wallace, A. M., Hoh, C. K., and Vera, D. R. (2012) Preoperative sentinel lymph node mapping of the prostate using PET/CT fusion imaging and Ga-68-labeled tilmanocept in an animal model. *Clinical & Experimental Metastasis 29*, 673−680.
(35) Morais, M., Paulo, A., Gano, L., Santos, I., and Correia, J. D. G. (2013) Target-specific Tc(CO)(3)-complexes for in vivo imaging. *J. Organomet. Chem. 744*, 125−139.
(36) Morais, M., Oliveira, B. L., Correia, J. D. G., Oliveira, M. C., Jimenez, M. A., Santos, I., and Raposinho, P. D. (2013) Influence of the bifunctional chelator on the pharmacokinetic properties of Tc-99m$(CO)_3$-labeled cyclic alpha-melanocyte stimulating hormone analog. *J. Med. Chem. 56*, 1961−1973.
(37) Morais, M., Raposinho, P. D., Oliveira, M. C., Pantoja-Uceda, D., Angeles Jimenez, M., Santos, I., and Correia, J. D. G. (2012) NMR structural analysis of MC1R-targeted rhenium(I) metallopeptides and biological evaluation of Tc-99m(I) congeners. *Organometallics 31*, 5929−5939.
(38) Wadas, T. J., Wong, E. H., Weisman, G. R., and Anderson, C. J. (2010) Coordinating radiometals of copper, gallium, indium, yttrium, and zirconium for PET and SPECT imaging of disease. *Chem. Rev. 110*, 2858−2902.
(39) Price, E., and Orvig, C. (2014) Matching chelators to radiometals for radiopharmaceuticals. *Chem. Soc. Rev. 43*, 260−290.
(40) Storr, T. (2014) *Ligand Design in Medicinal Inorganic Chemistry*; John Wiley & Sons: United Kingdom.
(41) Taylor, P., Gordon, S., and Martinez-Pomares, L. (2005) The mannose receptor: linking homeostasis and immunity through sugar recognition. *Trends Immunol. 26*, 104−110.
(42) Elzoghby, A. (2013) Gelatin-based nanoparticles as drug and gene delivery systems: Reviewing three decades of research. *J. Controlled Release 172*, 1075−1091.
(43) Wallace, A. M., Han, L. K., Povoski, S. P., Deck, K., Schneebaum, S., Hall, N. C., Hoh, C. K., Limmer, K. K., Krontiras, H., Frazier, T. G., Cox, C., Avisar, E., Faries, M., King, D. W., Christman, L., and Vera, D. R. (2013) Comparative evaluation of [Tc]tilmanocept for sentinel lymph node mapping in breast cancer patients: results of two phase 3 trials. *Ann. Surg. Oncol. 26*, 104−110.
(44) Keshtgar, M., Zaknun, J. J., Sabih, D., Lago, G., Cox, C. E., Leong, S. P. L., and Mariani, G. (2011) Implementing sentinel lymph node biopsy programs in developing countries: challenges and opportunities. *World Journal of Surgery 35*, 1159−1168.
(45) Scasnar, V., and Vanlier, J. E. (1993) The use of Sep-Pak SI cartridges for the preparation of gallium chloride from the citrate solution. *European Journal of Nuclear Medicine 20*, 273−273.
(46) Vera, D. R., Wallace, A. M., Hoh, C. K., and Mattrey, R. F. (2001) A synthetic macromolecule for sentinel node detection: (99m)Tc-DTPA-mannosyl-dextran. *J. Nucl. Med. 42*, 951−9.